

Washington University in St. Louis
Washington University Open Scholarship

All Theses and Dissertations (ETDs)

1-1-2011

Photoacoustic Tomography Of Water In Phantom And Biological Tissue

ZHUN XU

Follow this and additional works at: <https://openscholarship.wustl.edu/etd>

Recommended Citation

XU, ZHUN, "Photoacoustic Tomography Of Water In Phantom And Biological Tissue" (2011). *All Theses and Dissertations (ETDs)*. 841.
<https://openscholarship.wustl.edu/etd/841>

This Thesis is brought to you for free and open access by Washington University Open Scholarship. It has been accepted for inclusion in All Theses and Dissertations (ETDs) by an authorized administrator of Washington University Open Scholarship. For more information, please contact digital@wumail.wustl.edu.

WASHINGTON UNIVERSITY IN ST. LOUIS

School of Engineering and Applied Science

Department of Biomedical Engineering

Thesis Examination Committee:

Lihong Wang, Chair

Mark Anastasio

Yunan Xia

PHOTOACOUSTIC TOMOGRAPHY OF WATER IN PHANTOM AND
BIOLOGICAL TISSUE

by

Zhun Xu

A thesis presented to the School of Engineering
of Washington University in partial fulfillment of the
requirements for the degree of

MASTER OF SCIENCE

May 2011
Saint Louis, Missouri

copyright by

Zhun Xu

2011

ABSTRACT OF THE THESIS

Photoacoustic Tomography of Water in Phantom and Biological Tissue

by

Zhun Xu

Master of Science in Biomedical Engineering

Washington University in St. Louis, 2011

Research Advisor: Professor Lihong Wang

The concentration of water in the human body and tissue reflects both physiological and pathological properties. Photoacoustic tomography (PAT) has been widely used to image various tissues, with imaging contrast provided by many optical absorbers. However, to our knowledge, water has never been used as the absorption contrast in PAT. Herein, preliminary results of water detection and imaging with PAT are shown. The absorption spectra of water-ethanol mixtures with different water concentrations were photoacoustically measured, and the water content in both phantom and biological tissue was imaged. Finally, we present the results of *in vivo* PAT imaging of cold-injury induced water accumulation in the mouse brain, called cerebral edema.

Acknowledgments

This work was sponsored in part by National Institutes of Health grants R01 EB000712, EB000712A2S1, R01 EB00071207S2, R01 EB008085, R01 CA113453901, U54 CA136398, and 5P60 DK02057933. L.W. has a financial interest in Microphotoacoustics, Inc. and Endra, Inc., which, however, did not support this work.

I would like to thank the Dr. Wang for the project proposal and instruction. Special thanks go to the many graduate students and distinguished faculty members in my lab who have reviewed this thesis and helped support the related research.

Zhun Xu

Washington University in St. Louis

May 2011

Contents

| | |
|---|-----------|
| Abstract..... | ii |
| Acknowledgments..... | iii |
| List of Tables..... | v |
| List of Figures..... | vi |
| 1 Introduction..... | 1 |
| 1.1 Water..... | 1 |
| 1.2 Photoacoustic Tomography..... | 1 |
| 2 Theoretical Basis..... | 3 |
| 3 Spectral Measurements of Water–ethanol Mixtures by Photoacoustic Tomography..... | 5 |
| 3.1 Experimental Setup..... | 5 |
| 3.2 Results..... | 7 |
| 4. Water Content Imaging in Phantom and Biological Tissue..... | 10 |
| 4.1 Experimental Setup..... | 10 |
| 4.2 Results..... | 11 |
| 5. <i>In vivo</i> Imaging of Cerebral Edema by Photoacoustic Tomography..... | 14 |
| 5.1 Experimental Setup..... | 14 |
| 5.2 Results..... | 16 |
| 6. Conclusions..... | 19 |
| References..... | 20 |
| Vita..... | 22 |

List of Tables

Table 3.1: Comparison of water concentrations with corresponding PA-derived fractional values (5 means. For each mean, 100 PA signals were used)7

List of Figures

| | |
|--|----|
| Figure 3.1: Experimental setup of water–ethanol mixture spectrum measurement..... | 6 |
| Figure 3.2: Optical absorption coefficients from (a) photoacoustic measurements(five means. For each mean, 100 PA signals were used.) and (b) spectrophotometric measurements. Note that the 5% water solution is actually the ethanol stock solution. (c) Relative errors of the photoacoustic measurements from the spectrophotometric measurements at various wavelengths..... | 9 |
| Figure 4.1: Experimental setup of phantom and tissue experiment..... | 11 |
| Figure 4.2: Phantom experiment. (a) Photograph of a 4% agar gel with embedded objects of different water concentrations; (b) 2D photoacoustic image of the phantom. Squares: areas for signal integration and comparison. | 12 |
| Figure 4.3: Tissue experiment. (a) Photograph of fat tissue with an embedded 2% agar object; (b) 2D photoacoustic image of the fat tissue; (c) 1D PA signal along $y = -2$ mm. . . | 13 |
| Figure 5.1: Schematic of the photoacoustic tomography system for the <i>in vivo</i> experiment. | 15 |
| Figure 5.2: Transcranial photoacoustic images of the mouse brain acquired through the intact scalp and skull noninvasively acquired (a) before cold injury, (b) 12 hours after injury, and (c) 24 hours after injury. The upper and lower row images were acquired at 610 nm and 975 nm optical wavelengths, respectively. Three mice were imaged: two of them were kept alive until 36 hours after cold injury, and the third was sacrificed for MRI imaging 24 hours after the cold injury. (d) Integrated water and blood signal strengths in the dashed line area computed respectively for the three mice. The signal strengths were normalized to the water signal acquired before cold injury. (e) MRI image of the mouse cortex, taken immediately after the mouse was sacrificed (24 hours after cold injury). The edema is indicated by the arrow. The dashed line area in lower (c) outlines the contour area according to 60% of the maximum water signal acquired at 975 nm. | 17 |
| Figure 5.3: (a) – (d): Transcranial photoacoustic images acquired at 24 hours after cold injury at 925, 950, 1000, and 1025 nm wavelengths, respectively. The dashed line area is the same as the one shown in lower Fig. 2(c). (e) Comparison between the water absorption coefficients calculated by signal integrations in the reconstructed water accumulation region and the coefficients from spectrophotometric measurements. | 18 |

Chapter 1

Introduction

1.1 Water

The human body is composed of 60% water; the brain is nearly 70% water. The concentration of water in tissue may indicate different physiological and pathological properties, and several techniques have been applied to image water content in tissue. For instance, Magnetic Resonance Imaging (MRI) has been traditionally used to image water content in the brain^{1,2}, bone^{3,4} and other tissues^{5,6} based on its T2 contrast, and diffusion-weight MRI (DW-MRI) is used to map the bound water in brain and muscle tissues^{7,8}. Optical methods have also been used to measure the water content in tissues. For example, diffuse optical methods have been implemented to measure the increased water concentration in tumors⁹. Diffuse optical spectroscopy (DOS) can measure the spectral changes due to bound water¹⁰, yet its poor spatial location ability compromises its sensitivity¹¹.

1.2 Photoacoustic Tomography

Photoacoustic tomography (PAT) is a new and promising imaging technique in the biomedical field. When an object absorbs pulsed or intensity-modulated optical irradiation, acoustic waves are induced from transient thermoelastic expansion¹². PAT can reconstruct the absorption signals from the photoacoustic signals detected by the ultrasound transducer. It is capable of multi-scale imaging, from centimeter scale breast tumors to micrometer scale red blood cells¹³. Ultrasound detection

achieves useful penetration depths, while it keeps the features of optical imaging, such as high sensitivity and high resolution.

To date, the most important application of PAT is to image red blood vessels in various tissues in the mouse and human beings. Hemoglobin is the main absorption contrast in the blood vessel imaging. In addition, melanoma, and various natural and artificial contrast agents have also been used. Water has a local peak absorption coefficient of 0.45 cm^{-1} around 975 nm, with a FWHM of 920 nm – 1040 nm in the absorption spectrum¹⁴. However, water has never been used as the photoacoustic contrast. In this paper, we explore the potential of laser-based PA detection of water.

The next chapter briefly introduces the theoretical basis. Then, we describe how the absorption spectra of water–ethanol mixtures at various concentrations were measured by using the PA technique. After that, both phantom and tissue experiments to image water are detailed, and we also present the *in vivo* imaging of cerebral edema. Finally, conclusions and a discussion are provided.

Chapter 2

Theoretical Basis

The generation and propagation of a photoacoustic pressure wave in an acoustically homogenous and non-viscid infinite medium can be described as^{15,16}

$$\left(\nabla^2 - \frac{1}{v_s^2} \frac{\partial^2}{\partial t^2}\right)p(\mathbf{r}, t) = -\frac{\beta}{C_p} \frac{\partial}{\partial t} H(\mathbf{r}, t), \quad (1.1)$$

where $p(\mathbf{r}, t)$ denotes the acoustic pressure at position \mathbf{r} and time t , v_s is the speed of sound in the medium, β denotes the thermal coefficient of volume expansion, C_p denotes the isobaric specific heat capacity, and $H(\mathbf{r}, t)$ is the heating function (defined as the thermal energy converted at \mathbf{r} and t per unit volume and time). For optical absorption, the heating function generally equals $\eta_{th}\mu_a\Phi(\mathbf{r}, t)$, where η_{th} is the percentage of energy that is converted into heat, μ_a is the optical absorption coefficient, and Φ is the optical fluence rate.

In general, the initial pressure rise p_0 at \mathbf{r} immediately after illumination by a short laser pulse is given by¹⁷

$$p_0(\mathbf{r}) = \Gamma(\mathbf{r})\eta_{th}\mu_a(\mathbf{r})F(\mathbf{r}), \quad (2.2)$$

where $\Gamma = \frac{\beta v_s^2}{C_p}$ is defined as the Grueneisen coefficient (dimensionless), and F is the optical fluence. In many cases, η_{th} is approximately equal to one. The initial pressure

$p_0(\mathbf{r})$ is the source of the propagating PA pressure wave. It depends on not only the illumination fluence and absorption coefficient, but also on the Grueneisen coefficient. The dependence of the Grueneisen coefficient on the mixture's composition can be established by applying the formula $\Gamma = \frac{\beta v_s^2}{C_p}$. The values for the speed of sound, v_s , in water–ethanol mixtures with different water concentrations were obtained from Ref. 18. The thermal coefficient of volume expansion β , and specific heat capacity, C_p , of deionized water and pure ethanol were taken from Ref. 19.

The general image reconstruction for the initial pressure in an infinite acoustically homogenous medium was provided by Xu and Wang^{20,21}, which is described as

$$p_0^{(b)}(\mathbf{r}) = \frac{1}{\Omega_0} \int_s d\Omega [2p(\mathbf{r}_d, t) - 2t \frac{\partial p(\mathbf{r}_d, t)}{\partial t}] \Big|_{t=|\mathbf{r}_d-\mathbf{r}|/v_s}, \quad (2.3)$$

where $d\Omega = dS / |\mathbf{r} - \mathbf{r}_d|^2 \cdot [\mathbf{n}_d^s \cdot (\mathbf{r} - \mathbf{r}_d) / |\mathbf{r} - \mathbf{r}_d|]$ is defined as the infinitesimal solid angle at \mathbf{r}_d with respect to the reconstruction point \mathbf{r} . For our planar detection geometry, $\Omega_0 = 2\pi$. In our experiment, signals from 240 planar scanning positions were obtained. So the integration of equation (2.3) could be transformed into discrete form to get the reconstruction result.

Chapter 3

Spectral Measurements of Water–Ethanol Mixtures by Photoacoustic Tomography

In this chapter, we present our photoacoustic measurements of the optical absorption spectrum of water–ethanol mixtures. These measurements are compared with spectrophotometric measurements, which we selected as the gold standard.

3.1 Experimental Setup

Figure 3.1 shows the experimental setup of our absorption spectrum measurement system. A tunable laser (Vibrant (HE) 355 I, OPOTEK) was the light source. The repetition rate of the laser light was 10 Hz. The wavelength was selected with the range of 925-1025 nm, covering the local peak absorption of water. For each experiment, a thin-walled plastic container with a preset constant volume of water–ethanol mixture was placed above a 2.25 MHz unfocused ultrasonic transducer (V323, Panametrics). The transducer was immersed in a tank of mineral oil during the experiment. The distance from the bottom surface of the mixture to the front surface of the transducer was ~ 2 cm. Here we used the peak-to-peak PA signal value to represent $p_0(\mathbf{r})$. The signal from the transducer was amplified by 40 dB by a pulse amplifier (5072 PR, Panametrics) and then delivered to and recorded by a data acquisition card (CompuScope 14100, GaGe, Lockport, IL). The sampling rate of the data acquisition card was 50 MHz.

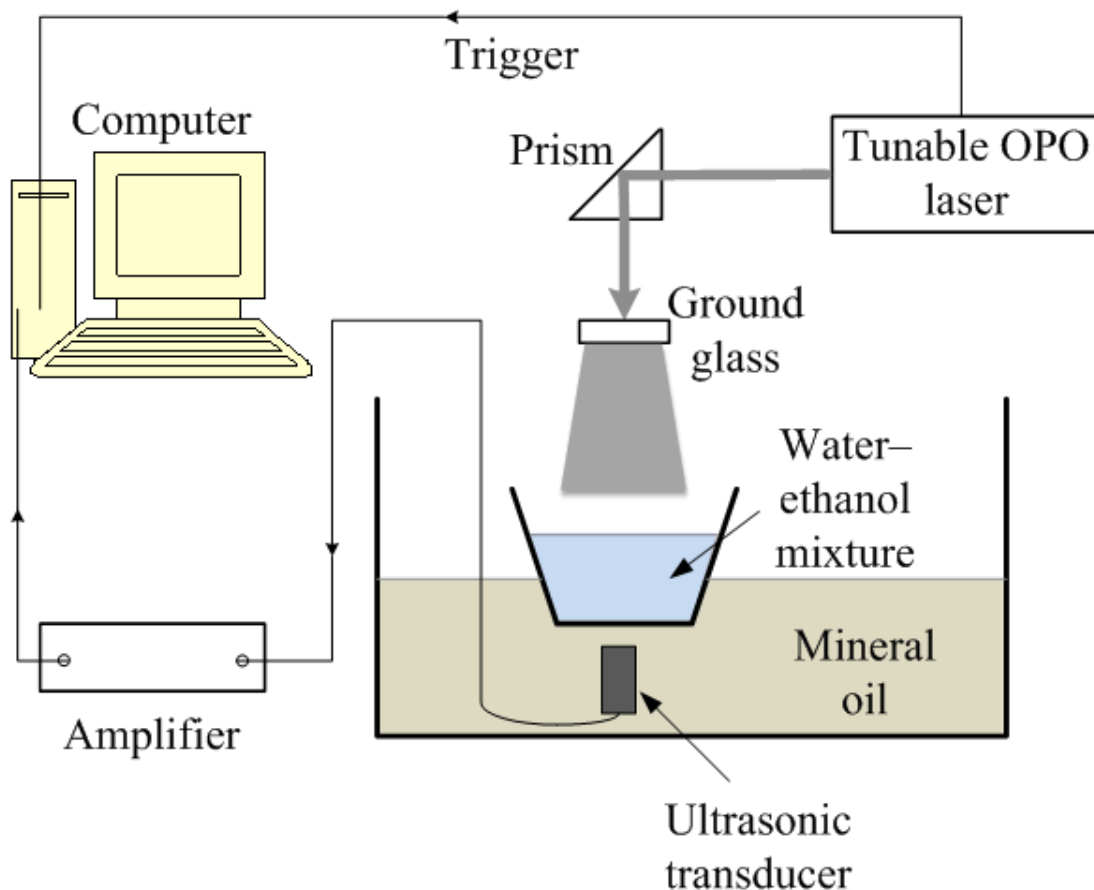


Figure 3.1 Experimental setup of water-ethanol mixture spectrum measurement

Six mixtures of water-ethanol with different volume concentrations of water were made: 100% (pure deionized water), 80%, 60%, 40%, 20%, and 0% (ethanol only). Since the ethanol used was 95% pure (Pharmco-Aaper, 190 Proof) with the remaining 5% being water, the actual volume concentrations of water were 100%, 81%, 62%, 43%, 24% and 5%, respectively. The laser power was calibrated in the spectral range from 925 nm to 1025 nm at intervals of 25 nm. The laser pulse energy was recorded by a powermeter (Melles Griot broadband power/energy meter 13PEM001), with 20 laser pulses averaged at each wavelength.

3.2 Results

Based on the assumption that the absorption coefficient varies linearly with the water volume concentration, and using the linear fit of the Grueneisen coefficient obtained by the method shown in chapter 3.1, we can get a quadratic dependence of the PA signal with the water concentration (figure not shown here). The quadratic character of the curve indicates that the water fraction of a water–ethanol mixture is non-monotonic and might not be determined uniquely according to the PA measurement alone. In general, one PA signal corresponds to two possible water concentrations. The exception is for the mixture with 50% water concentration. We measured relative PA signals at the 975 nm wavelength for five different mixtures, and estimated the water concentration according to the quadratic dependence. Results are listed in Table 3.1.

Table 3.1. Comparison of water concentrations with corresponding PA-derived fractional values (five means. For each mean, 100 PA signals were used)

| Preset water concentration | 10% | 30% | 50% | 70% | 90% |
|--|--------------|--------------|-------|--------------|--------------|
| Photoacoustically measured water concentration (solution 1) | 8.5% ± 0.4% | 30.3% ± 1.1% | 50.6% | 72.2% ± 0.8% | 89.0% ± 0.5% |
| Photoacoustically measured water concentration (solution 2) | 92.7% ± 0.4% | 70.9% ± 1.1% | 50.6% | 28.9% ± 0.8% | 12.1% ± 0.5% |

The relative absorption spectra were computed with Eq. (2.2) and then converted to absolute values (Figure 3.2 (a)) by calibrating with the absorption coefficient of deionized water at 975 nm measured by a spectrophotometer (Cary 5E, Varian, Walnut Creek, CA). For Eq. (2.2), we used the Grueneisen coefficient and the calibrated and uniformly distributed optical fluence. For comparison, the absorption spectra were also measured with the spectrophotometer as a gold standard (Figure 3.2 (b)). The relative errors between the PA and spectrophotometric data are plotted in Figure 3.2 (c), which basically shows good accordance. Yet at 925 nm the error is relatively large due to water's small absorption coefficient at that wavelength.

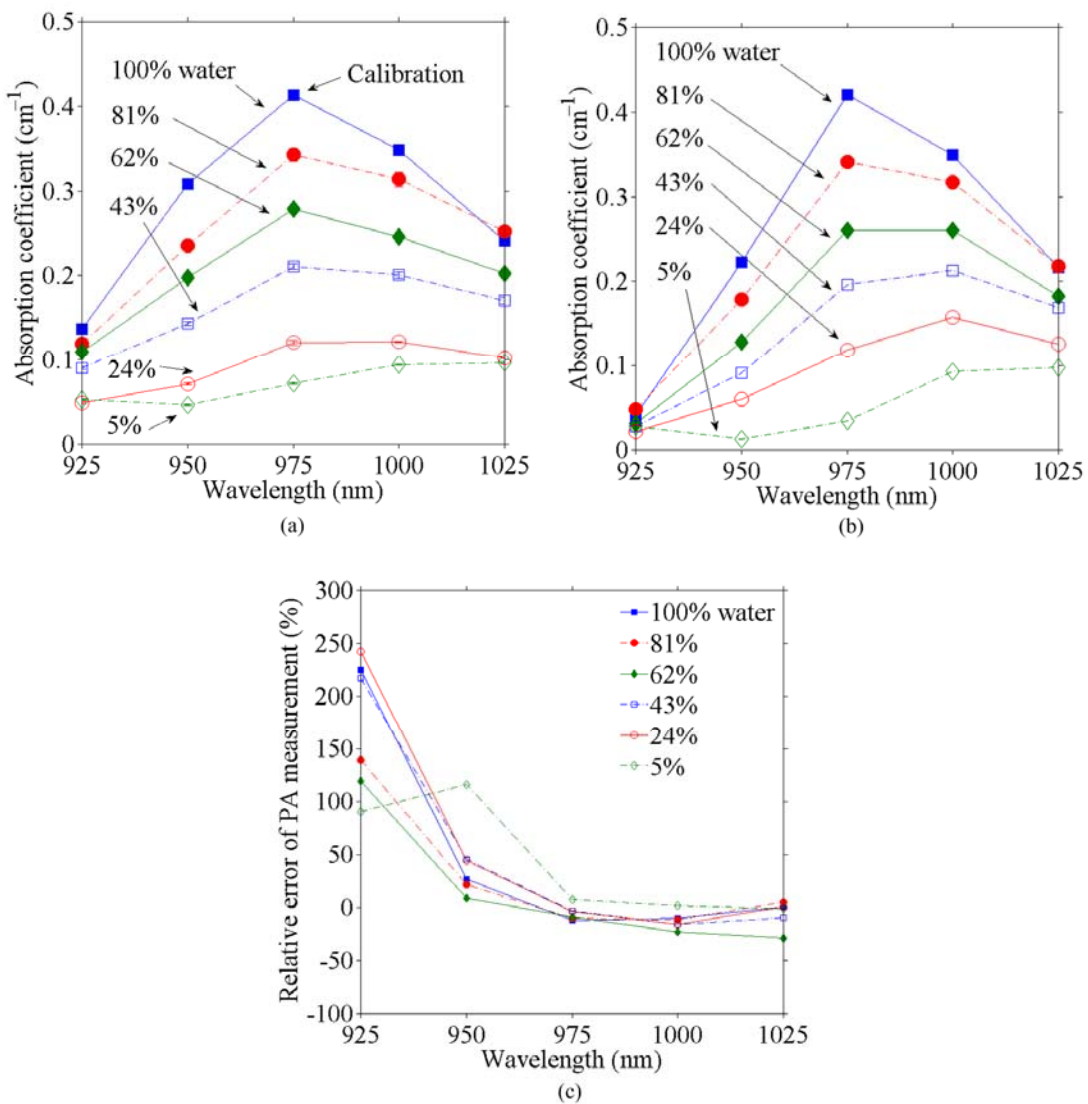


Figure 3.2 Optical absorption coefficients from (a) photoacoustic measurements (five means. For each mean, 100 PA signals were used.) and (b) spectrophotometric measurements. Note that the 5% water solution is actually the ethanol stock solution. (c) Relative errors of the photoacoustic measurements from the spectrophotometric measurements at various wavelengths.

Chapter 4

Water Content Imaging in Phantom and Biological Tissue

4.1 Experimental Setup

Figure 4.1 shows the experimental setup for the phantom and biological tissue experiment. Similar to the spectrum measurement setup, the only difference was the single-element transducer ((842-300, GE) with a center frequency of 2.25 MHz) placed beside the imaging object and immersed in mineral oil in the tank. During the imaging process, the transducer was rotated around the object through 240 positions evenly distributed along the horizontal scanning trajectory in order to get a full view of the photoacoustic signals. The image reconstruction was implemented in the computer after data acquisition, using the image reconstruction algorithm described in Chapter 2.

Two samples were imaged using this PAT system. For sample 1, a gel cylinder made of an agar–water mixture (4% agar) was used. Three 5 mm diameter cylindrical holes were dug in the gel cylinder. One hole was filled with deionized water, another with 40% ethanol–60% deionized water mixture, and the third hole was left empty (Figure 4.2 (a)). For sample 2, a piece of porcine fat was used as the background. A hole was drilled in the fat and filled with 2% agar gel (Figure 4.3 (a)). The wavelength for the imaging was selected as 975 nm.

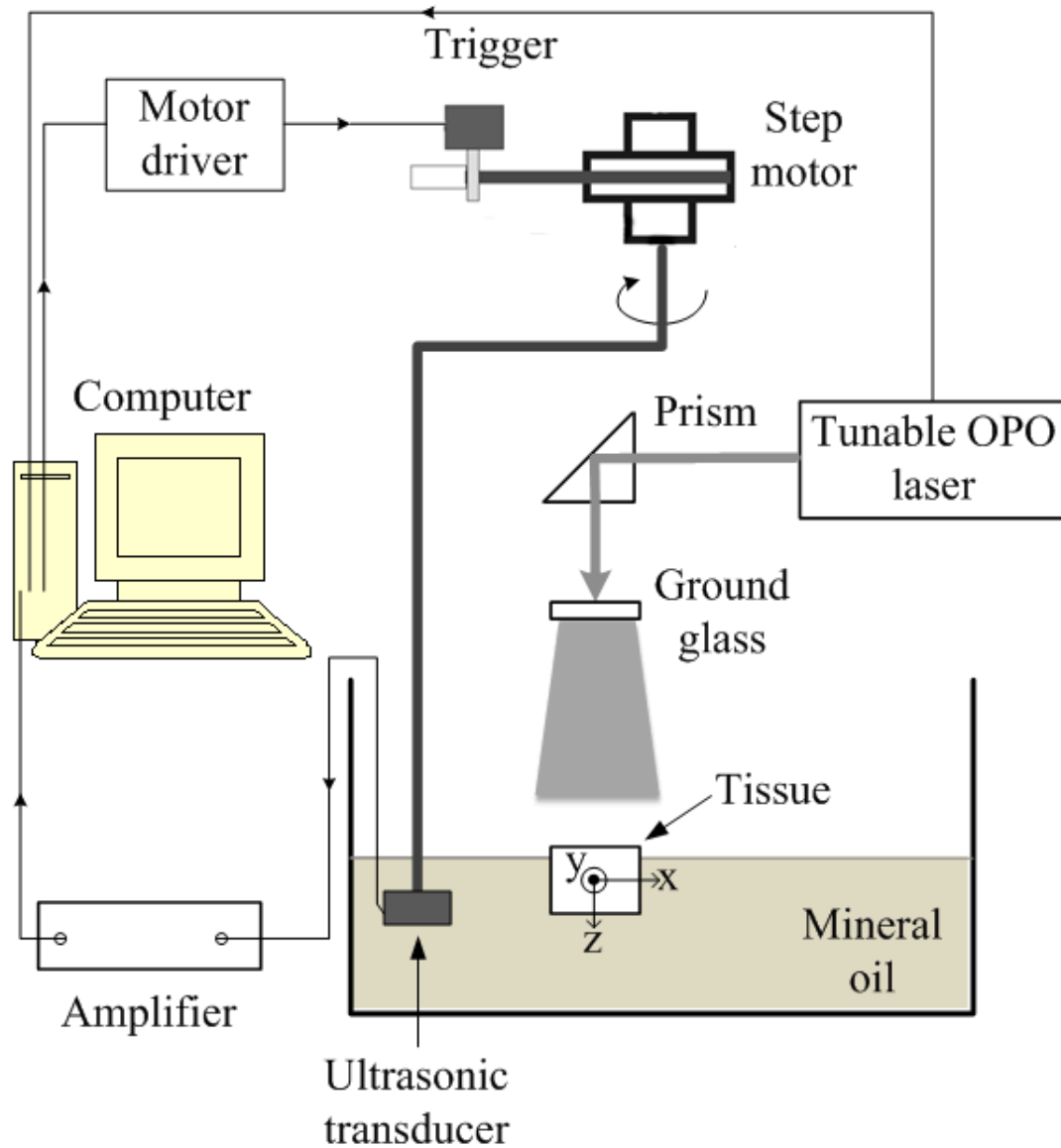


Figure 4.1 Experimental setup of phantom and tissue experiment

4.2 Results

Figure 4.2 shows a PAT image of objects with different water concentrations at 975 nm. The negative value is partially due to the limited bandwidth of the ultrasonic detection system. In the quantitative study of PA signal in Chapter 5, we added a positivity constraint during the iterative process in the reconstruction to eliminate the

negative values. The reconstructed signal was integrated within the two squares marked in Figure 4.2 (b). The 40% water–60% ethanol mixture yielded a higher PA signal than deionized water, and the ratio was consistent with the quadratic dependence described in Chapter 3.

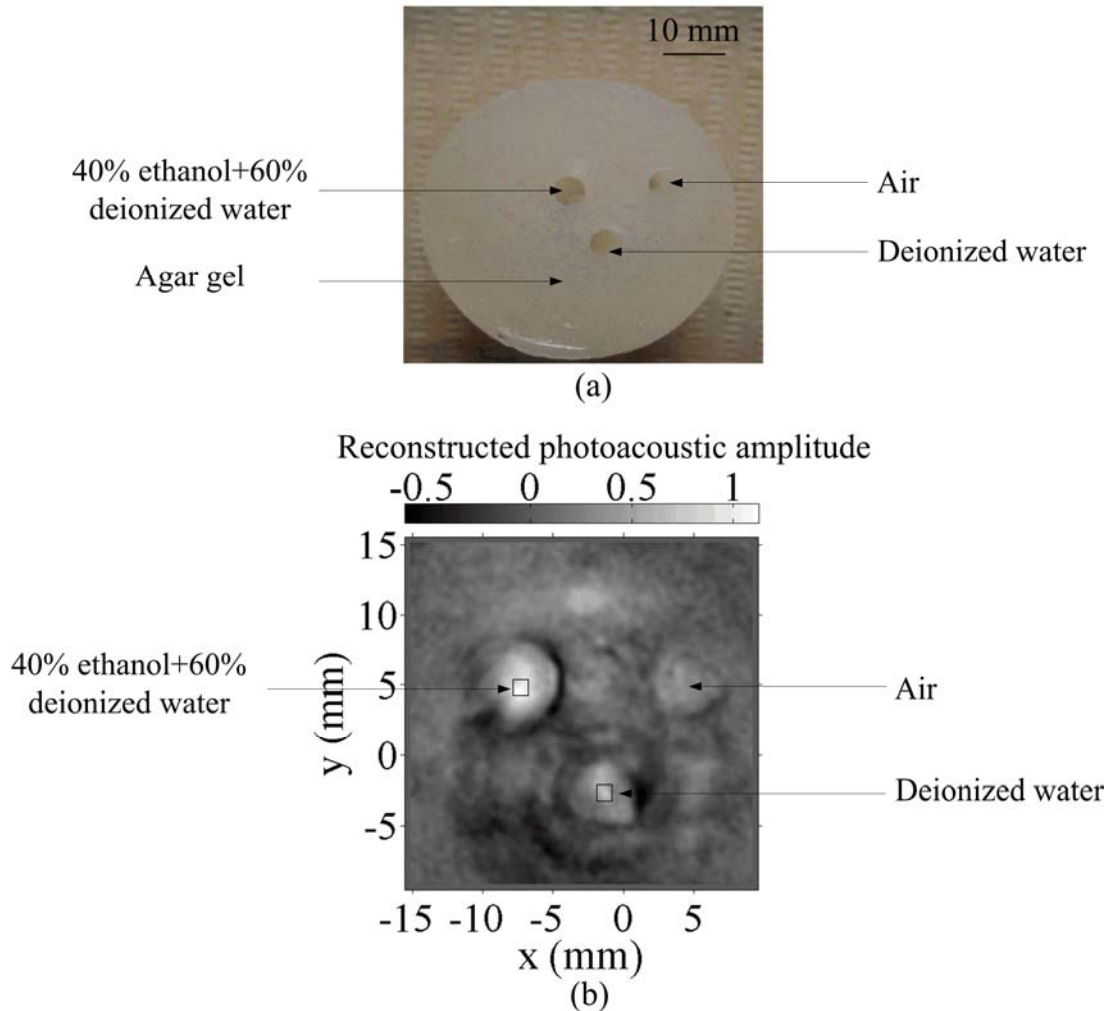


Figure 4.2. Phantom experiment. (a) Photograph of a 4% agar gel with embedded objects of different water concentrations; (b) 2D photoacoustic image of the phantom. Squares: areas for signal integration and comparison.

The tissue experiment (Figure. 4.3 (b)) indicated that water generates nine times stronger PA signals than fat at the 975 nm wavelength (Figure 4.3 (c)). Both the absorption coefficient and the Grueneisen coefficient may account for such a signal difference between water and fat. Thus, PAT has great potential to detect localized water in fat.

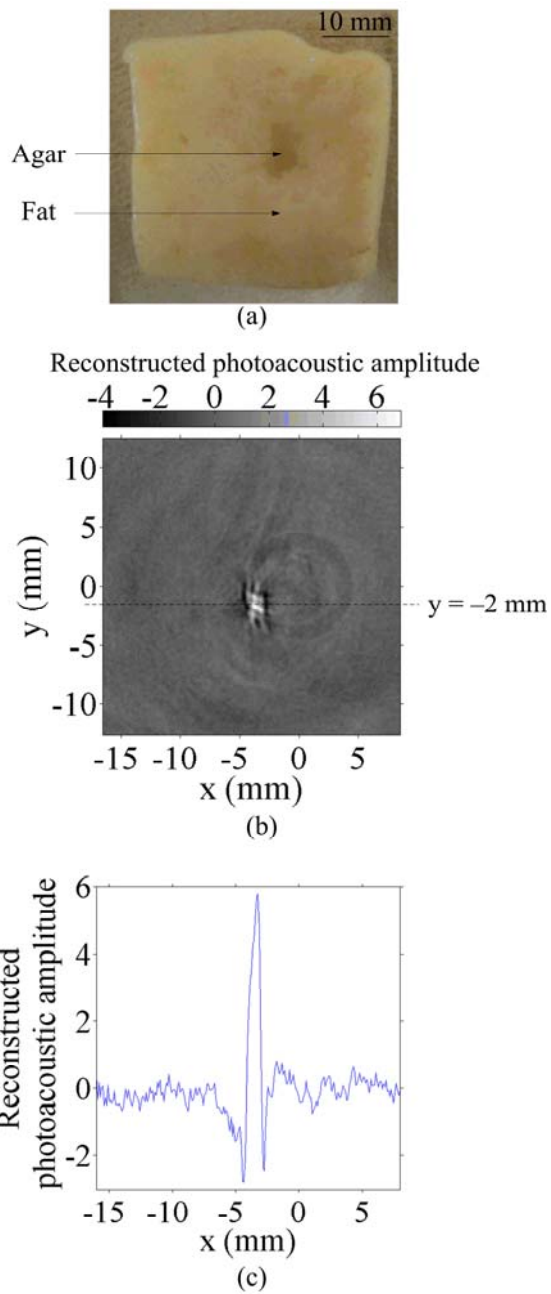


Figure 4.3. Tissue experiment. (a) Photograph of fat tissue with an embedded 2% agar object; (b) 2D photoacoustic image of the fat tissue; (c) 1D PA signal along $y = -2$ mm.

Chapter 5

In vivo Imaging of Cerebral Edema by Photoacoustic Tomography

5.1 Experimental Setup

Figure 5.1 shows the real-time experimental setup for the *in vivo* study. Two wavelengths, 610 nm and 975 nm, were used to image a mouse brain *in vivo*. A ground glass homogenized the laser beam, making it evenly distributed on the brain surface. The fluence of each laser pulse on the surface was lower than the American National Standards Institute (ANSI) safety standard (20 mJ/cm^2). A 512-element full-ring array was inserted in the system served as the ultrasonic detector. The central frequency of the transducer was 5 MHz, and it took 16 seconds to obtain one cross-sectional image with 10-times averaging.

The mouse was anesthetized during the experiment. Cold-induced cerebral edema was generated by putting a liquid nitrogen-filled aluminum tube in contact with the mouse scalp for ~30 seconds. The animal remained on the experimental stage for the entire duration of imaging. Three animals were used for the experiment. For two of the animals, changes in blood flow volume and water accumulation at the edema site were tracked 12, 24, and 36 hours after the cold injury by obtaining the photoacoustic imaging of the brain cortex. For the third animal, only changes at 12

and 24 hours after the cold injury were tracked. After that, the mouse was sacrificed and an MRI *ex vivo* image of the cortex was taken immediately. The whole procedure follows the rules in Animal Studies Protocol Compliance.

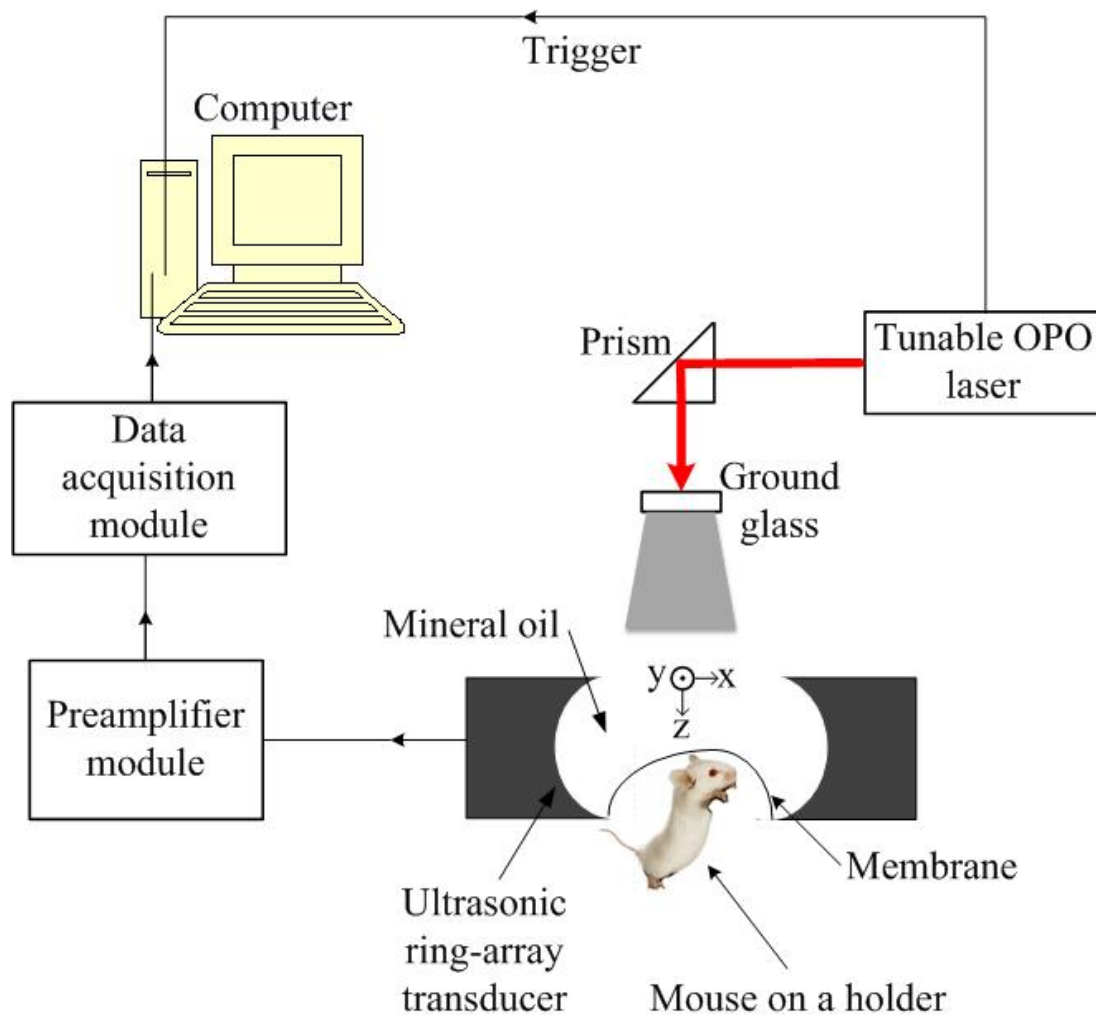


Figure 5.1 Schematic of the photoacoustic tomography system for the in vivo experiment.

The solid-angle-weighted image reconstruction algorithm developed by Li et al.²¹ was used for the image reconstruction. As mentioned in Chapter 3, the iterative

algorithm was applied²² and the positivity constraint was added during each iterative step so as to eliminate the negative signals due to the bandwidth limitation.

5.2 Results

Figure 5.2 shows the brain images acquired *in vivo* by PAT at both 610 nm and 975 nm and subsequently acquired *ex vivo* by MRI. The upper images in Figure 5.2 (a) – (c) indicate that the amount of blood in the vessel decreased during the first 24 hours after the cold injury. The lower images show an accumulation of water after the cold injury. The maximum size of the water accumulation region was observed at 24 hours after the cold injury. The T2-weighted MRI image (shown in Figure 5.2 (e)) validated such region as an edema. Figure 5.2 (d) shows the integrated signals of both blood and water. The dashed line encircled contour at 60% of the maximum pixel value represents the region of the edema (Figure 5.2 (c)). From the bar plot in Figure 5.2 (d), we can see that 36 hours after the cold injury, both PA signals of water and blood returned to the original levels, indicating the recovery of the mouse.

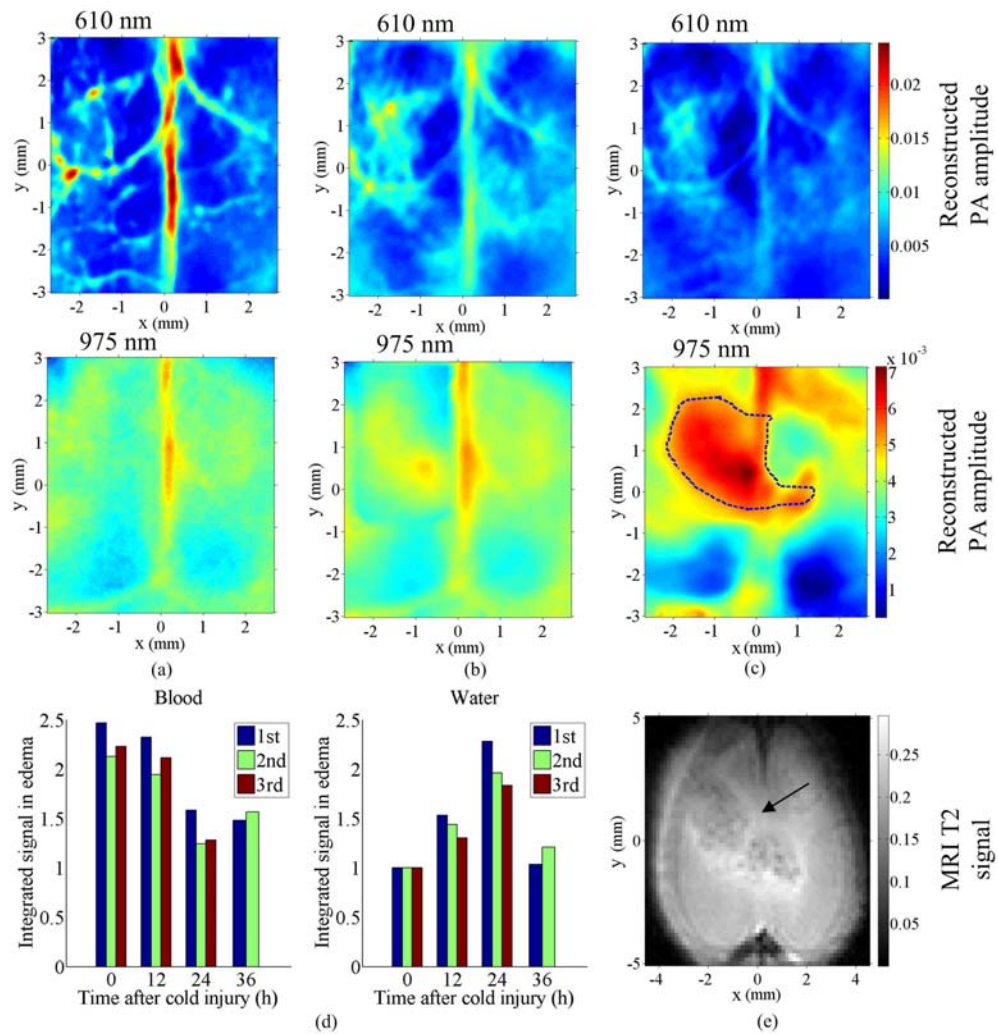


Figure 5.2 Transcranial photoacoustic images of the mouse brain acquired through the intact scalp and skull noninvasively acquired (a) before cold injury, (b) 12 hours after injury, and (c) 24 hours after injury. The upper and lower row images were acquired at 610 nm and 975 nm optical wavelengths, respectively. Three mice were imaged: two of them were kept alive until 36 hours after cold injury, and the third was sacrificed 24 hours after the cold injury for MRI imaging. (d) Integrated water and blood signal strengths in the dashed line area computed respectively for the three mice. The signal strengths were normalized to the water signal acquired before cold injury. (e) MRI image of the mouse cortex, taken immediately after the mouse was sacrificed (24 hours after cold injury). The edema is indicated by the arrow. The dashed line area in lower (c) outlines the contour area according to 60% of the maximum water signal acquired at 975 nm.

The signals in the water accumulation region were also integrated with the images obtained at five different wavelengths: 925 nm, 950 nm, 975 nm, 1000 nm, and 1025 nm (images shown in Fig. 3 (a) – (d)). Again, the spectrophotometric

measurement was used as the gold standard. The comparison with the expected water absorption is shown in Figure 5.3 (e).

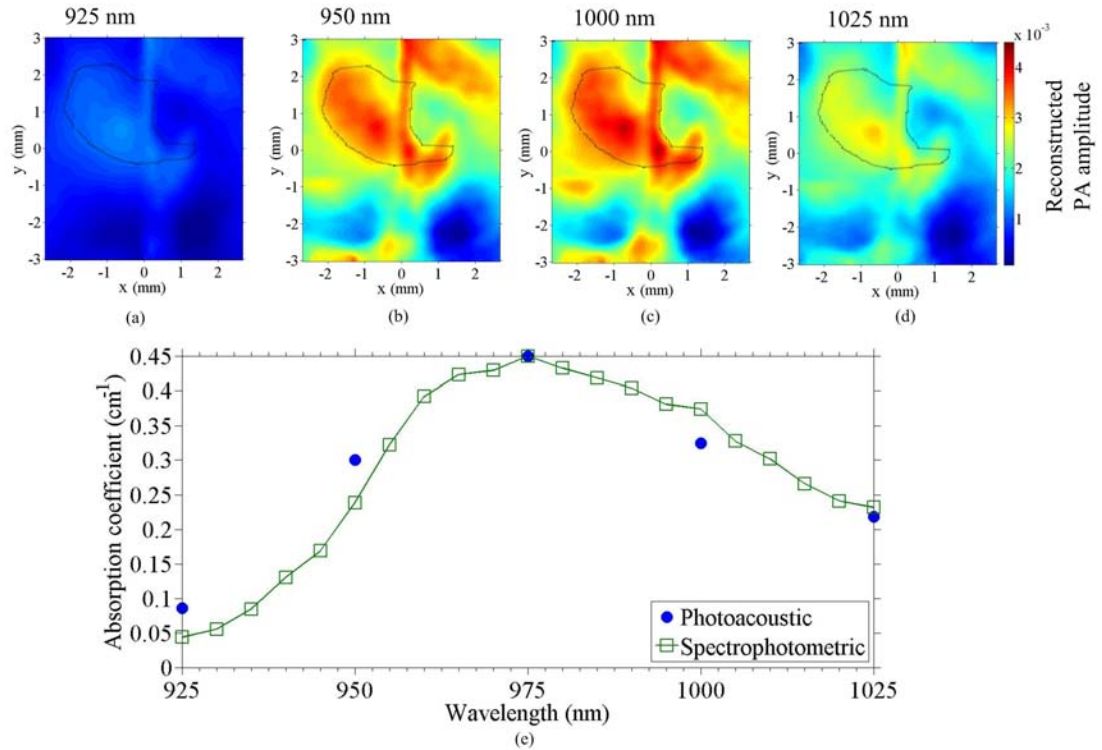


Figure 5.3 (a) – (d): Transcranial photoacoustic images acquired at 24 hours after cold injury at 925, 950, 1000, and 1025 nm wavelengths, respectively. The dashed line area is the same as the one shown in lower Fig. 2(c). (e) Comparison between the water absorption coefficients calculated by signal integrations in the reconstructed water accumulation region and the coefficients from spectrophotometric measurements.

Chapter 6

Conclusions

We have demonstrated the potential for water detection and imaging with photoacoustic tomography. First we photoacoustically measured the optical absorption coefficients of the water content in six water–ethanol mixtures. The linear dependence of the PA signal on the water concentration indicated the ability of PA to detect absorption detection. Then our phantom and tissue experiments showed that we could not only detect but also image water content in tissue, especially water in tissue with very low water concentration, as we showed in Chapter 4. Finally, we imaged the water content *in vivo* in the mouse brain. The formation of cerebral edema and its expansion and recovery was monitored with PAT. The results of the photoacoustic approach demonstrated its ability to image the cold–induced cerebral edema and its potential to image water. PAT required less time than MRI to obtain the image of water. Moreover, PAT is non-invasive and doesn't require injected contrast agents, which allows it to outperform perfusion methods. Our results in water imaging with PAT make it possible to accurately differentiate several contrasts and monitor the corresponding physiological parameters with more optical wavelengths.

References

- [1] D. J. Brooks, P. Luthert, D. Gadian and C. D. Marsden, "Does Signal-Attenuation on High-Field T2-Weighted MRI of the Brain Reflect Regional Cerebral Iron Deposition - Observations on the Relationship between Regional Cerebral Water Proton T2 Values and Iron Levels," *Journal of Neurology, Neurosurgery and Psychiatry* 52(1), 108-111, 1989.
- [2] R. Kreis, T. Ernst and B. D. Ross, "Development of the Human Brain - in-Vivo Quantification of Metabolite and Water-Content with Proton Magnetic-Resonance Spectroscopy," *Magnetic Resonance in Medicine* 30(4), 424-437, 1993.
- [3] P. Fantazzini, R. Viola, S. M. Alnaimi and J. H. Strange, "Combined MR-relaxation and MR-cryoporometry in the study of bone microstructure," *Magnetic Resonance Imaging* 19(3-4), 481-484, 2001.
- [4] X. D. Wang and Q. W. Ni, "Determination of cortical bone porosity and pore size distribution using a low field pulsed NMR approach," *Journal of Orthopaedic Research* 21(2), 312-319, 2003.
- [5] R. Mathurdevre, "Biomedical Implications of the Relaxation Behavior of Water Related to NMR Imaging," *British Journal of Radiology* 57(683), 955-976, 1984.
- [6] F. Mirrashed and J. C. Sharp, "In vivo morphological characterisation of skin by MRI micro-imaging methods," *Skin Research and Technology* 10(3), 149-160, 2004.
- [7] P. J. Basser, J. Mattiello and D. LeBihan, "Mr Diffusion Tensor Spectroscopy and Imaging," *Biophysical Journal* 66(1), 259-267, 1994
- [8] J. V. Hajnal, M. Doran, A. S. Hall, A. G. Collins, A. Oatridge, J. M. Pennock, I. R. Young and G. M. Bydder, "Mr Imaging of Anisotropically Restricted Diffusion of Water in the Nervous-System - Technical, Anatomic, and Pathological Considerations," *Journal of Computer Assisted Tomography* 15(1), 1-18, 1991.
- [9] A. Cerussi, N. Shah, D. Hsiang, A. Durkin, J. Butler and B. J. Tromberg, "In vivo absorption, scattering, and physiologic properties of 58 malignant breast tumors determined by broadband diffuse optical spectroscopy," *Journal of Biomedical Optics* 11(4), -, 2006.

- [10] J. B. Brubach, A. Mermet, A. Filabozzi, A. Gerschel and P. Roy, "Signatures of the hydrogen bonding in the infrared bands of water," *Journal of Chemical Physics* 122(18), -, 2005.
- [11] S. H. Chung, A. E. Cerussi, C. Klifa, H. M. Baek, O. Birgul, G. Gulsen, S. I. Merritt, D. Hsiang and B. J. Tromberg, "In vivo water state measurements in breast cancer using broadband diffuse optical spectroscopy," *Physics in Medicine and Biology* 53(23), 6713-6727, 2008.
- [12] L. V. Wang, "Multiscale photoacoustic microscopy and computed tomography," *Nature Photonics* 3(9), 503-509, 2009.
- [13] L. H. V. Wang, "Prospects of photoacoustic tomography," *Medical Physics* 35 (12), 5758-5767, 2008.
- [14] G. M. Hale, M. R. Querry, "Optical constants of water in the 200 nm to 200 μ m wavelength region," *Appl. Opt.*, (12), 555-563, 1973.
- [15] P. M. Morse and K. U. Ingard, *Theoretical acoustics*, McGraw-Hill, New York, 1968.
- [16] G. J. Diebold, T. Sun and M. I. Khan, "Photoacoustic Monopole Radiation in 1-Dimension, 2-Dimension, and 3-Dimension," *Physical Review Letters* 67(24), 3384-3387, 1991.
- [17] L. V. Wang, "Tutorial on photoacoustic microscopy and computed tomography," *Ieee Journal of Selected Topics in Quantum Electronics* 14(1), 171-179, 2008.
- [18] H. Hobæk, Å. Voll, R. Fardal and L. Calise, "Experiment on Finite Amplitude Sound Propagation in a Fluid with a Strong Sound Speed Gradient," *AIP Conference Proceedings* 838(1), 593-600, 2006.
- [19] H. D. Young, R. M. Geller and F. W. Sears, *Sears & Zemansky's college physics*, Pearson/Addison Wesley, San Francisco, 2007.
- [20] M. H. Xu and L. V. Wang, "Universal back-projection algorithm for photoacoustic computed tomography," *Physical Review E* 75(5), -, 2007.
- [21] C. H. Li and L. H. V. Wang, "Photoacoustic tomography of the mouse cerebral cortex with a high-numerical-aperture-based virtual point detector," *Journal of Biomedical Optics* 14(2), -, 2009.
- [22] Z. J. Guo, C. H. Li, L. A. Song and L. H. V. Wang, "Compressed sensing in photoacoustic tomography in vivo," *Journal of Biomedical Optics* 15(2), -, 2010.

Vita

Zhun Xu

- Date of Birth** March 10, 1985
- Place of Birth** Beijing, P.R.China
- Degrees** B.S. Tsinghua University, Biomedical Engineering, July 2007
M.S. Tsinghua University, Biomedical Engineering, July 2009
M.S. Washington University in St.Louis, Biomedical Engineering,
anticipated May 2011
- Publications** Zhun Xu, Changhui Li, Lihong Wang. (2010)
Photoacoustic tomography of water in phantoms and tissue,
Journal of Biomedical Optics. 15(3): 036019.
- Zhun Xu, Changhui Li, Lihong Wang. (2011)
Photoacoustic tomography of water in biological tissue, *SPIE
Proceedings* Vol. 7899.

May 2011